3D statistical analysis of a copper powder sintering observed in situ by synchrotron microtomography

Alexander Vagnon, J.P. Rivière, Jean-Michel Missiaen, D. Bellet, Marco Di Michiel, Charles Josserond, Didier Bouvard

To cite this version:

Alexander Vagnon, J.P. Rivière, Jean-Michel Missiaen, D. Bellet, Marco Di Michiel, et al.. 3D statistical analysis of a copper powder sintering observed in situ by synchrotron microtomography. Acta Materialia, 2008, 56 (5), pp.1084-1093. 10.1016/j.actamat.2007.11.008 . hal-00142266

3D statistical analysis of a copper powder sintering observed in situ by synchrotron microtomography

A. Vagnon [a], J.P. Rivière [a], J.M. Missiaen [a,*], D. Bellet [a], M. Di Michiel [b], C. Josserond [a], D. Bouvard [a]

[a] *SIMAP, Laboratoire de Science et Ingénierie des Matériaux et Procédés, Grenoble INP-CNRS-UJF, Domaine Universitaire, BP 75, 38402 Saint-Martin d'Hères, France*
[b] *European Synchrotron Radiation Facilities (ESRF), BP 220, 38043 Grenoble cedex, France*

Sintering of a copper spherical powder was observed in situ by X-ray microtomography at the European Synchrotron Radiation Facility. Morphological tools have been developed to obtain three-dimensional (3D) quantitative microstructural characteristics of the particle packing. The average microstructural changes (neck size, coordination number, pore size distribution) and the macroscopic densification are in agreement with the predictions of the mean field sintering models, which assume a uniform shrinkage of the powder compact. The present 3D results confirm that the effect of the inherent heterogeneity of a random dense particle packing on the average microstructural changes during sintering is limited.

Keywords: 3D image analysis; Heterogeneity; Microtomography; Particle packing; Rearrangement

1. Introduction

Sintering is the consolidation of a powder compact which results from a thermal treatment at a temperature where the specimen is mainly solid, so that the shape of the compact is essentially maintained. Microstructural descriptions of sintering often use a model consisting of two particles ("2-Sphere model") or a characteristic coordination polyhedron of the particles (Voronoï cell or regular polyhedron), which is assumed to represent the average local microstructure of the particle compact. Assuming that shrinkage is uniform throughout the compact, the macroscopic shrinkage is then deduced from its expression at the local scale (mean field approach). This was the case in the early sintering models that were developed in the 1950s [1–4], but also in further developments aimed at taking into account simultaneous mass transport mechanisms, or to give a more realistic geometrical description than the early models [5,6]. This is also the case in numerical models later developed to deduce constitutive equations for sintering materials [7–10]. Such descriptions do not account for microstructural heterogeneity that may generate non-uniform particle displacements at the scale of the particle packing. In the ideal situation of regular particle packing, the particle centre-to-centre distance or the pore volume will decrease in the same way in every local cell. In contrast, dispersion of the local shrinkage and densification is expected in random packing due to the inherent heterogeneity of the packing configurations. The question then is how this can disturb the average microstructure variation and the average shrinkage or densification kinetics. This is an important issue, since it concerns not only average predictions of the mean field models, but also the validity of the constitutive equations derived from microstructural models which are used to investigate the effect of macroscopic heterogeneities from continuum mechanics [11–13].

---

[*] Corresponding author.
E-mail address: missiaen@ltpcm.inpg.fr (J.M. Missiaen).

Experimental characterization of the effect of microstructural heterogeneity on sintering has been performed on two-dimensional (2D) arrays [14–16]. Weiser and De Jonghe [16] quantified the dispersion of local densification rates in Voronoï cells of the packing. They found a direct correlation between the average rate of interparticle angular changes and the standard deviation of local densification rates. Rearrangement of the particle packing is then driven by the stresses generated due to differential shrinkage and is directly correlated to the microstructural heterogeneity. Local pore opening between regions of high density is often observed in such experiments in the initial stage of sintering. It is closely related to the packing heterogeneity, and then to the initial packing density: in denser arrays, large pores shrink and their area decreases similarly to the decrease in the area of small pores, whereas in the less dense arrays large pores can grow considerably larger than their original size [15]. Experimental characterization of three-dimensional packings is usually performed on 2D sections, where information on the 3D particle neighbourhood cannot be accessed [17,18] unless serial sections are used [19]. Moreover, investigating changes with time is only possible from different post-mortem samples, since the 2D section analysis is destructive. The 3D pore size distribution can be analysed on post-mortem samples by using undirect physical methods, such as mercury penetration [20–22], gas desorption, or X-ray/neutron small-angle scattering [23]. These analyses often report the growth of intermediate size pores in the early stage of sintering in the case of heterogeneous or low-density green samples [20,22,23], like in the 2D observations. This pore growth can result from differential shrinkage, but it can also be related to the existence of a critical pore size for curvature driven mass transport [24].

However, very few experimental studies deal with the effect of microstructural heterogeneity on sintering by direct 3D analysis. 3D analysis of microstructural changes in a true particle packing undergoing sintering is hard to implement. Numerical experiments by discrete element models (DEM) may help to deal with those aspects, since they can account for rearrangement of the particle packing [25–29]. The first DEM results concerning sintering of spherical particles tend to indicate that the effect of microstructural heterogeneity on the change in particle coordination and on neck growth and densification kinetics remains limited in a random close particle packing [28,29]. Recent progress in X-ray tomography allows for the direct 3D observation of microstructural changes during sintering of a powder compact [30–33]. This technique permits, for the first time, the changes in the local neighbourhood configurations to be followed during sintering. The effects of the natural heterogeneity of a powder particle packing can then be analysed directly. Very few quantitative results using this technique have been published to date. Sintering of a copper powder packing was observed in situ by synchrotron microtomography [30]. A 3D statistical analysis of the microstructure changes during these experiments is presented here. The aim of this paper is to investigate the influence of microstructural heterogeneity on the variation of average microstructural characteristics, such as local densities, neck sizes, pore size distribution and coordination numbers, and on the sintering kinetics. The results are discussed and compared with the common predictions of mean field models, which assume uniform shrinkage of the powder compact throughout sintering. A dense random particle packing is considered for this first approach, in order to determine if variations of average characteristics of the packing may deviate from mean field predictions in a system where heterogeneity is limited, but present, with reference to a uniform regular packing where the mean field assumption is trivial.

2. Experiments

A packing of spherical copper particles with diameters between 40 and 60 μm was investigated. The powder was poured into a quartz capillary, 1 mm in diameter and 20 mm in height, and gently tapped. The capillary was then introduced into a furnace specially designed at the European Synchrotron Radiation Facility (ESRF) for in situ microtomography (Fig. 1). Sintering was performed in a He/H_2 atmosphere, with the thermal cycle reported in Fig. 2. For each data set, 900 X-ray radiographies of the specimen were recorded at different rotation angles, covering an interval of 180°. For the data correction, dark fields (a measurement of the detector background) and flat fields (images of the X-ray beam without sample) were also recorded. The exposure time was 0.05 s per image. A com-

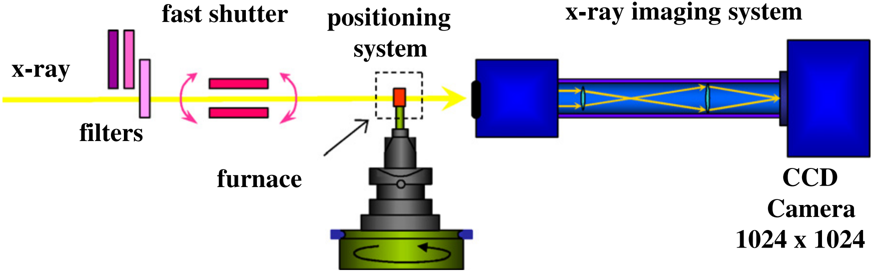

Fig. 1. Microtomography set-up at ESRF ID15 beam line.

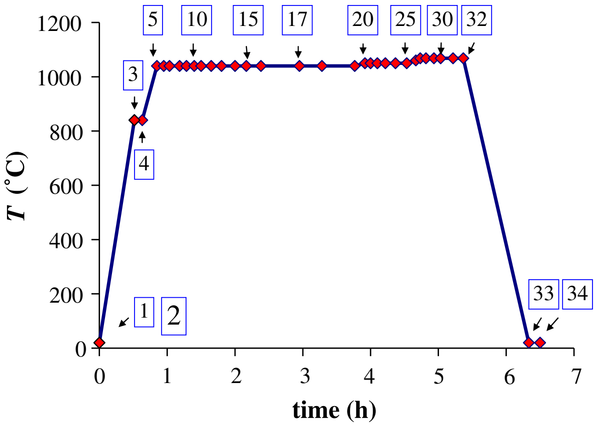

Fig. 2. Full thermal schedule imposed to the copper powder (microtomographies are marked and numbered on the graph).

plete set of radiographies with a resolution close to 2 μm could be collected in about 1 min. Local variation of the microstructure during collection time is below the resolution limit. Other details of the experiments can be found in Refs. [30,31].

Data collection was performed at different stages of the thermal schedule, as indicated in Fig. 2. 3D volumes with (600 × 600 × 255) voxels of (1.6 × 1.6 × 1.6 μm) were reconstructed by applying a standard filtered back-projection algorithm to the 2D images. The sample is expected to move slightly between microtomography collections, due to both thermal expansion and sintering shrinkage. To ensure that we were really investigating the same sample volume, the measured volume was shifted in the vertical direction from one microtomograph to the other. In order to follow the local microstructural variations, (600 × 600 × 85) 3D volumes centred on the same horizontal slice were extracted from the complete volumes. These volumes, hereafter called reference volumes, contained a few hundred particles and were processed and analysed using specific programs developed with the Amira™ and Aphelion™ image analysis software packages. Automatic image processing ensured a reproducible method for extracting the solid phase from the raw images, for the segmentation of particles and for the determination of microstructural characteristics. Image processing and measurement techniques are detailed below. Fig. 3a is a view of the 3D particle compact and Fig. 3b represents a set of reconstructed particles showing interparticle necks.

2.1. Image processing

Shading effects were corrected by multiplying the intensities at each point x in the volume by the ratio $I(x_{\text{center}})/I(x)$, where $I(x)$ is the local average intensity in the solid phase and $I(x_{\text{center}})$ is the particular value at the centre of the volume. $I(x)$ function was obtained by a morphological closing of the initial image. Automatic thresholding of the greytone image was then performed by a deconvolution of histogram peaks, to get a binary image representing the solid phase (voxel intensity = 1 in the solid phase and 0 in the pore phase).

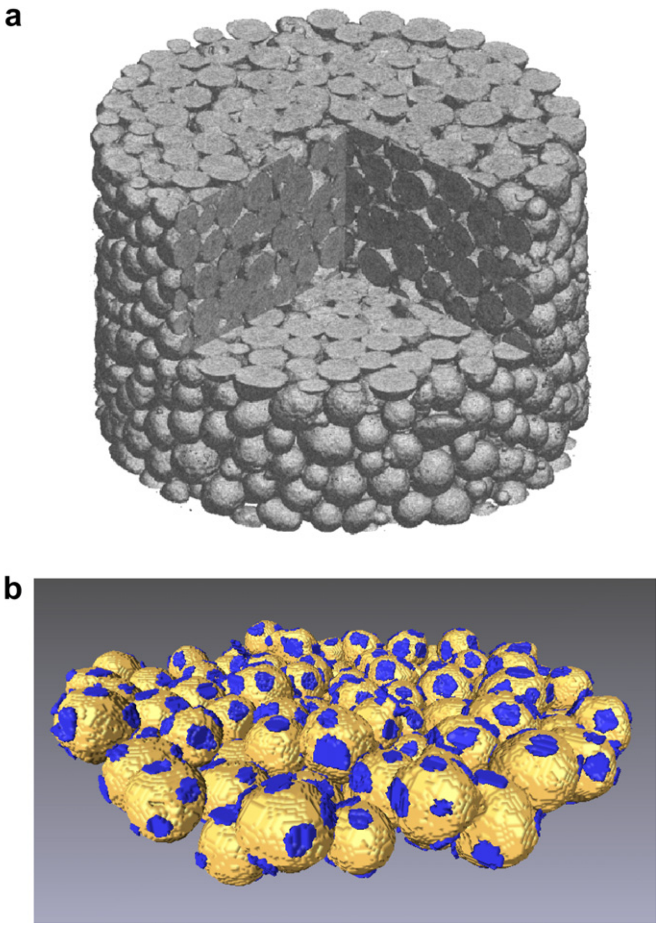

Fig. 3. (a) A view inside the 3D reconstructed image of the copper compact before sintering (microtomography 1 in Fig. 2) and (b) a set of extracted particles at the beginning of sintering (microtomography 3 in Fig. 2) showing interparticle necks.

2.2. Edge effects on the measurements

Edge effects were corrected by the usual procedure used for 2D images: (i) in the case of measurement on individual objects (particles), the measurement is restricted to those objects whose centre is inside the reduced volume obtained by erosion of the packing envelope with a size equal to the maximum object radius; and (ii) in the case of measurements resulting from a morphological transformation, the measurement is restricted to the reduced volume obtained by erosion of the packing envelope with a size equal to that of the structuring element used for the transformation ("theorem of the frame of measurements" [34]).

2.3. Basic measurements

Basic parameters, such as volume fractions, mean intercepts in each phase and specific surface areas, were obtained by automatic image analysis, by extending the standard stereological techniques used in the 2D image analysis [34,35]. The volume fraction V_V was estimated through the voxel fraction N_P. The number of intercepts was obtained by counting local (0 1) voxel configurations (voxels whose value is 1 and having a left-neighbour voxel whose value is 0). The mean intercept L_1 was deduced from the ratio of the voxel fraction to the number of intercepts per unit length N_L in a given volume:

$$L_l = \frac{N_P}{N_L} \tag{1}$$

The surface area per unit volume S_V was estimated from the number of intercepts per unit length:

$$S_V = 4N_L \tag{2}$$

Using stereological concepts in a 3D space where the whole information is a priori accessible is questionable. The advantages of such a procedure is that it is based on an analysis of local voxel configurations and therefore: (i) it does not require to precise the exact position of phase boundaries by a polygonization of the particle borders and (ii) edge effects can be more easily dealed with. This procedure is valid if one can assume that the digitization process (acquisition of 2D radiographies; mathematical reconstruction of the 3D volumes; thresholding of the copper phase) acts as a stochastic sampling of the particles in the volume: voxels with a value equal to 1 in the binary image correspond to points which are actually inside particles, whereas voxels with a value equal to 0 correspond to points which are in the void space. Hence, although the exact position of phase boundaries is not determined, an unbiased statistical estimation of morphological characteristics such as the total volume or surface of a phase can be performed in the digitized space.

2.4. Analysis of the solid and pore phases with mathematical morphology tools

Granulometry by morphological opening gives the volume fraction of a set into which a geometric element of a given size and shape can be included [34,36]. The intercept length distributions in the solid phase and in the pore phase were computed by morphological openings with linear segments as structuring elements. If $g(l)$ stands for the distribution density, $g(l)\mathrm{d}l$ represents the volume fraction of the phase having a length between l and $l + \mathrm{d}l$ in the direction of analysis. The volume fractions are usually given with respect to the total volume of the phase, so that the distribution is normalized. In addition to this normalized distribution, a modified distribution density $g'(l)$ was used for the pore phase by expressing volume fractions with respect to the volume of the solid phase:

$$g'(l) = g(l)\frac{1 - V_V\ (\mathrm{Solid})}{V_V\ (\mathrm{Solid})} \tag{3}$$

where V_V (Solid) is the solid volume fraction in the compact (fractional density). The so-defined distribution density represents the actual pore volume in each size class by unit solid volume and is then equal, to within one constant factor, to the absolute pore volume in each size class.

2.5. Particle segmentation

Particle segmentation is necessary to analyse the particle and neck size distributions, and the particle coordination numbers and neighbourhood. Automatic segmentation was performed by adapting a procedure of watershed of the distance function [37,38] (see Fig. 4). The distance function was first calculated (Fig. 4b). This function is a grey level representation of the distance to particle edges. The watershed of the negative of this function was then computed by a flooding process (Fig. 4d). "Catching basins" were obtained, which represent the cells of influence of each particle in the image (set of points which are closer to one particle than to all other particles). The frontiers of these cells were deduced by thresholding (Fig. 4e) and substracted to the binary image to separate particles (Fig. 4f).

2.6. Particle and neck size measurements – coordination numbers

A set of labelled particles was reconstructed from the segmented image. The number of particles per unit volume N_V was determined from the number of particle centres inside the reduced volume for correction of edge effects. The volume V_S of each particle was computed, with the assumption of stochastic digitization discussed above, i.e. by simply multiplying the number of voxels in each particle by the unit voxel volume. An equivalent sphere radius R was determined:

$$R = \left(\frac{3V_S}{4\pi}\right)^{1/3} \tag{4}$$

A set of links between particles in contact was settled by a reconstruction of the labelled particles situated at a distance lower than the voxel size of a given particle. The coordination number of each particle and the average coordination number Z of the particle packing were deduced.

Necks between particles were obtained by a logical difference between the non-segmented and segmented images and a set of labelled necks were reconstructed. Fig. 3b shows a set of particles with their superimposed necks. Analysis of the neck sizes requires associating the necks and the particles that they separate. In particular, we have to distinguish between necks separating two particles and those separating three or more particles, which may have a much more complex shape. The particles in contact with each labelled neck were first reconstructed. Only necks in contact with two particles were then analysed. The apparent volumes V_N of digitized necks were computed by multiplying the number of voxels in each neck by the unit voxel volume. An equivalent disk radius x was then determined for each neck:

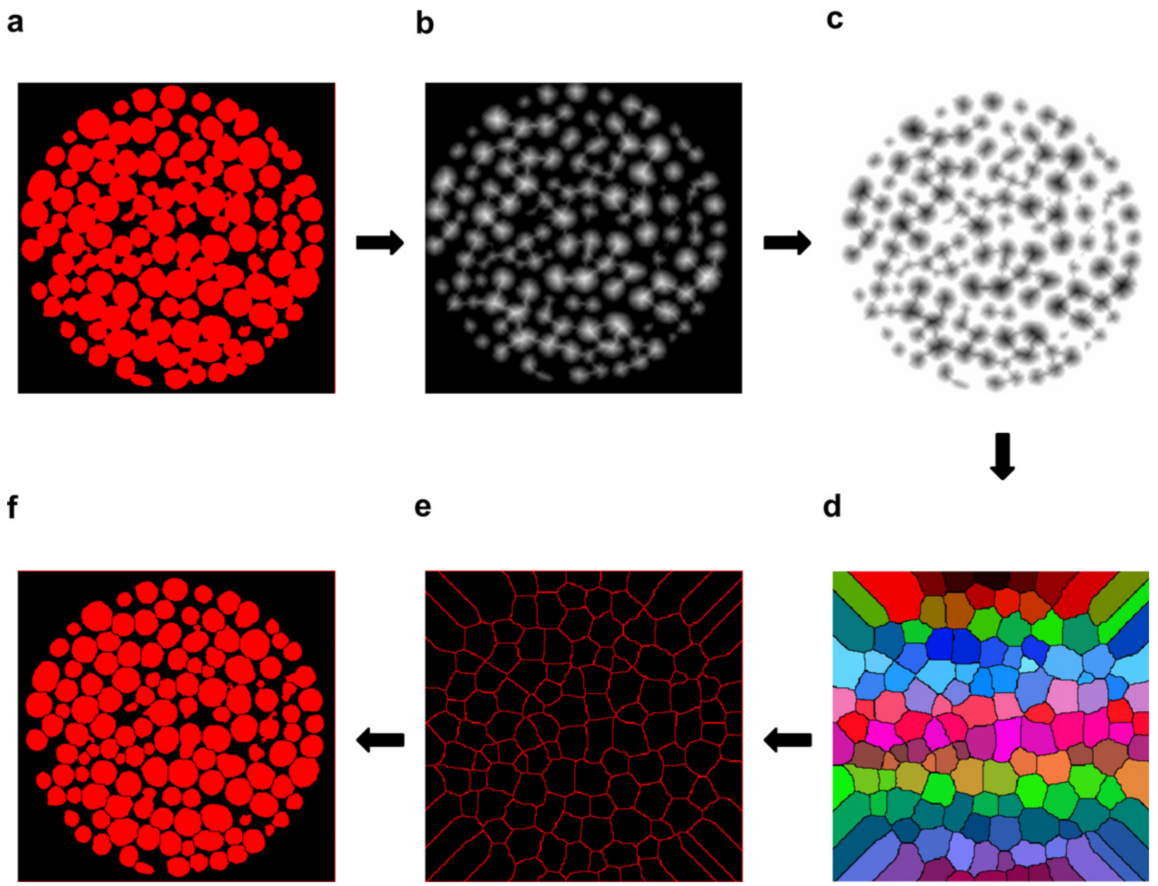

Fig. 4. 2D representation of the main steps used for 3D particle segmentation: (a) binary image of copper; (b) greytone image of the distance function; (c) inversion; (d) watershed; (e) thresholding; (f) substraction to the initial image.

$$x = \left(\frac{V_N}{\pi p}\right)^{1/2} \tag{5}$$

where p is the voxel size. The most frequent neck radius was determined from the peak in the measured neck size distribution. The most frequent size was preferred to the mean size, since elimination of necks in contact with more than two particles results in a gradual elimination of the larger necks, and the mean value would not concern the same population throughout sintering. The resolution in the analysis of neck sizes is poor due to digitization. Indeed, surface points distant by less than twice the voxel size will appear in contact in the images. The minimum detectable contact radius $x_{\min}$ for particles with radius R is then given by:

$$\frac{x_{\min}}{R} \approx \sqrt{\frac{2p}{R}} \tag{6}$$

$x_{\min}/R$ is about 0.36 for spheres of average radius ($R = 25$ μm) in point contact, with our digitizing conditions ($p = 1.6$ μm). This value gives the average resolution limit in the analysis of neck sizes.

The average neck size was also determined from the specific surface area of grain boundaries S_V (Solid:Solid). This surface area was obtained by substracting the solid/pore surface area S_V (Pores)-measured on the non-segmented image-of the total specific surface area of particles S_V (Particles)-measured on the segmented image:

$$S_V\ (\text{Solid} : \text{Solid}) = \frac{1}{2}(S_V\ (\text{Particles}) - S_V\ (\text{Pores})) \tag{7}$$

The average neck area a is then deduced:

$$a = \frac{S_V\ (\text{Solid} : \text{Solid})}{N_V Z/2} \tag{8}$$

The equivalent neck radius x_S is:

$$x_S = \sqrt{\frac{a}{\pi}} \tag{9}$$

This global analysis of the average neck size does not distinguish between necks separating two particles and those separating three or more particles, which induces a bias in the determination of an equivalent radius from Eq. (9).

2.7. *Porosity dispersion*

The watershed operation (see particle segmentation) was also used to analyse the dispersion of local densities or local porosities, by measuring the volume fraction of

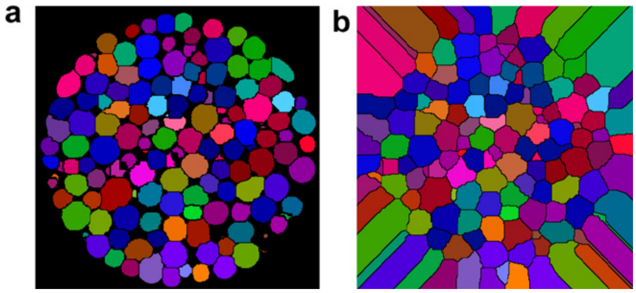

Fig. 5. 2D sections representing separated grains (a) and their influence cells obtained through the watershed operation (b).

particles or pores inside the cells of influence of each particle (Fig. 5).

3. Results

Analysis of the local (600 × 600 × 85) reference volume was performed from 840 to 1070 °C (microtomographies 3–32 in Fig. 2).

The results are plotted vs. a dimensionless time τ defined from the sintering kinetic models for neck growth [39]:

$$(x/R)^n = \tau \tag{10}$$

The advantage of using a dimensionless time is that the whole heating schedule can be taken into account by a numerical calculation of the integrated dimensionless time $\int d\tau$ at each point of the thermal schedule. Expressions of τ and n were taken from the kinetic equations of the 2-Sphere model derived in Ref. [39], in the case of surface (τ_S), grain boundary (τ_B) or volume diffusion (τ_V) control (Table 1). A modified kinetic model (from Ref. [40]), which takes into account the compressive stress at the center of the necks, was also used for comparison. The stress gradient at the surface of the neck is four times larger in this calculation and mass transport from the grain boundary is then much more rapid. Data for diffusion coefficients and surface tension of copper were taken from Ref. [41].

Table 1
Expressions of the dimensionless time τ and exponent n for neck growth kinetic Eq. (10) controlled by surface, grain boundary or volume diffusion

	Dimensionless time τ (from Ref. [39])	Dimensionless time τ (modified from Ref. [40])	Kinetic
exponent *n*			
Surface diffusion	$\frac{56\delta_S D_S \gamma \Omega}{kTR^4} t$	–	7
Grain boundary diffusion	$\frac{48\delta_B D_B \gamma \Omega}{kTR^4} t$	$\frac{192\delta_B D_B \gamma \Omega}{kTR^4} t$	6
Volume diffusion (from grain boundary)	$\frac{16 D_V \gamma \Omega}{kTR^3} t$	$\frac{64 D_V \gamma \Omega}{kTR^3} t$	4

δ_S and δ_B are, respectively, the width of the surface and grain boundary diffusion layer; D_S, D_B and D_V are, respectively, the surface, grain boundary and volume diffusion coefficient; γ is the surface tension, Ω the atomic volume, k the Boltzmann constant, T the temperature, R the sphere radius and t the time (from Refs. [39,40]).

The neck to grain radius ratio x/R is represented as a function of every dimensionless time in Fig. 6. The neck size values determined from the analysis of individual necks and from the global estimation of the specific surface area of grain boundaries (Eq. (9)) are plotted for comparison. The average resolution limit discussed above is also reported on the graph. The measured average neck radius is stationary at the beginning of sintering, as long as the actual value is lower than the resolution limit, and then it increases. From comparison with the models (Eq. (10)), it can be deduced that surface diffusion is the dominant mechanism for neck growth in our experimental conditions, at least as long as surface curvature gradients are present. The grain boundary diffusion contribution is, however, significant, and is responsible for shrinkage and densification. Unfortunately, information on contact

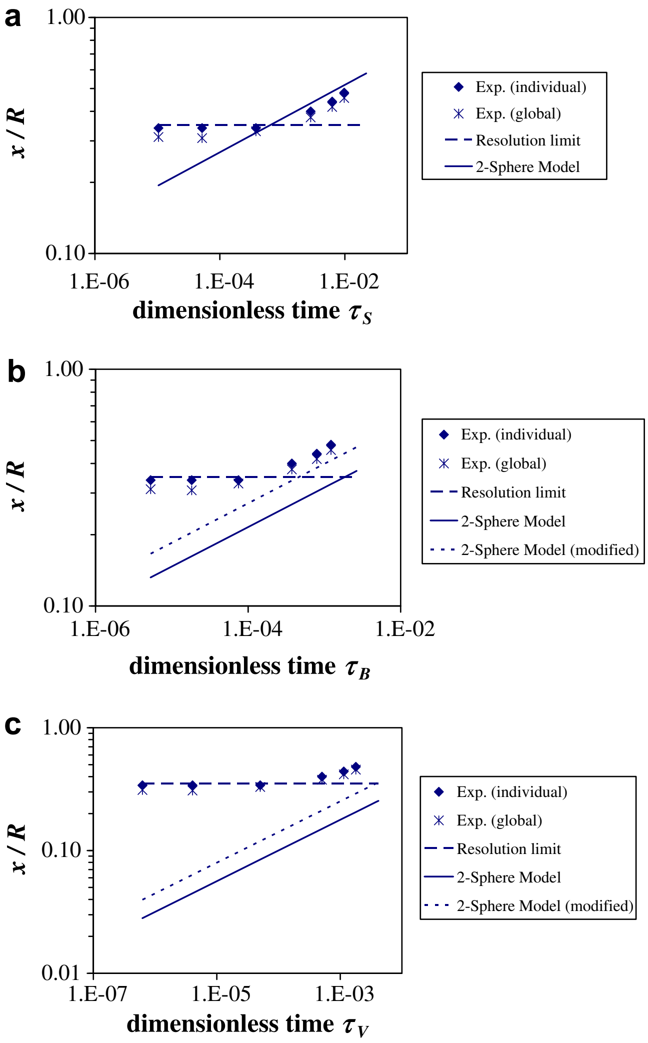

Fig. 6. Experimental and theoretical ratio x/R of the average neck radius x to the average particle radius R as a function of the sintering dimensionless time τ_S for surface diffusion (a), τ_B for grain boundary diffusion (b) or τ_V for volume diffusion (c).

formation and possible contact breaking cannot be deduced from the neck size distribution due to the limited resolution on the smaller necks.

The fractional density increases from 70% to 82% of the theoretical density in the range of analysis. This can be compared with the prediction of conventional 2-Sphere sintering models by using the relation between the fractional density ρ and the linear shrinkage ε:

$$\rho = \frac{\rho_0}{(1+\epsilon)^3} \tag{11}$$

where ρ_0 is the fractional green density. The linear shrinkage ε can be expressed as a function of the fractional neck size in 2-Sphere sintering models for mass transport mechanisms inducing shrinkage [39]:

$$\epsilon = -\frac{1}{4}\left(\frac{x}{R}\right)^2 \tag{12}$$

The fractional neck size is related to the dimensionless time τ from Eq. (10). The fractional density was calculated with Eqs. (11), (12) and (10) using the data of Table 1 for grain boundary diffusion control and volume diffusion control. The experimental and theoretical values are plotted in Fig. 7 as a function of the corresponding dimensionless times. Experimental densities obtained on complete volumes are also plotted on the same graph to check that the reference volume is representative of the packing. The fit between experimental and theoretical values is quite good in the case of grain boundary diffusion control, and it can be concluded that this mechanism is the main mass transport mechanism for densification.

The mean intercept length in the Cu grains remains constant throughout sintering (Fig. 8a). The grain size distribution is nearly unchanged (Fig. 8b), with only the elimination of the finest particles at the beginning of sintering, and the average particle radius remains equal to 25 μm throughout the whole sintering process. Grain growth is then very limited in our experimental conditions.

The mean intercept length in the pore phase L_1 (Pores) also remains nearly constant (Fig. 8a). This means that the effect of the size reduction of the largest porous channels on the mean pore intercept is compensated for by the closure of the finest channels. This is consistent with the common observation that the specific surface area S_V linearly decreases with the solid volume fraction V_V (Solid) in the intermediate stage of sintering [19,35,42,43]. Indeed,

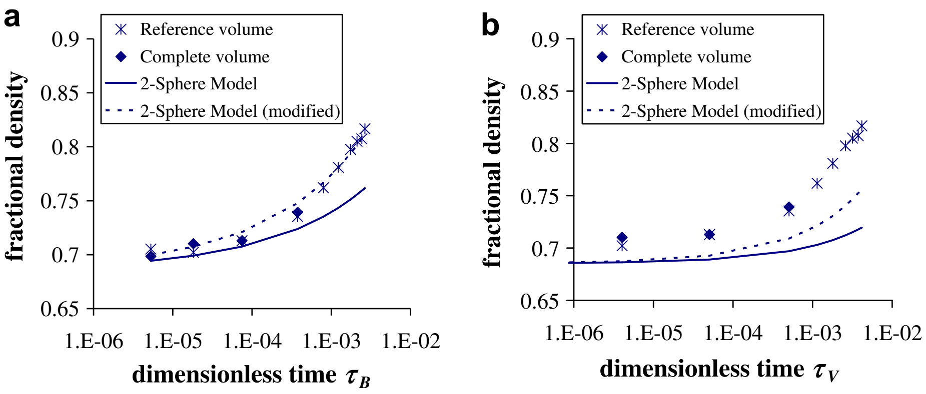

Fig. 7. Fractional density as a function of the dimensionless time and corresponding 2-Sphere calculations for: (a) grain boundary diffusion control and (b) volume diffusion control.

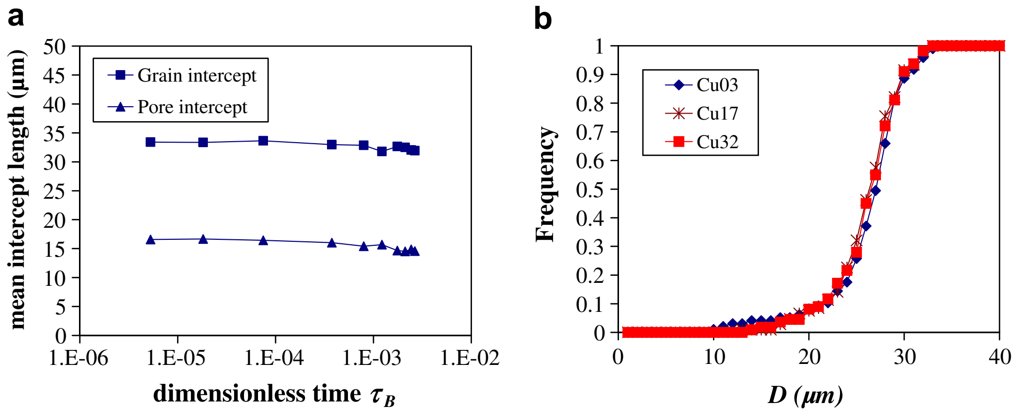

Fig. 8. (a) Mean intercept lengths in copper grains and in the pore phase as a function of the dimensionless time τ_B for grain boundary diffusion. (b) Cumulative grain size distribution at different stages of sintering (the numbers correspond to the microtomographies referred to in Fig. 2).

from stereological relations, the slope of the $S_V(V_V)$ plot is simply related to the mean pore intercept [44]:

$$S_V = \frac{4}{L_1\ (\text{Pores})}(1 - V_V\ (\text{Solid})) \tag{13}$$

The mean coordination number Z increases during sintering, due to the formation of new contacts as particles get closer to one another (Fig. 9a). This increase can be related to the average number of neighbours at distance d in a close particle packing of equal spheres [45]:

$$Z = Z_0 + 15.5\frac{\Delta d}{2R} \tag{14}$$

where $\Delta d = d - 2R$ is the inter-particle spacing and $Z_0 \approx 7.3$ is the average coordination number in the initial packing. Indeed, due to the resolution limit discussed above, surface points that are less than twice the voxel size apart will appear in contact in the images. The measured coordination number is then systematically overestimated and a first-order expression of the error can be deduced from Eq. (14):

$$\Delta Z \approx 15.5\frac{2p}{2R} \tag{15}$$

This gives an overestimation $\Delta Z \approx 1$ in our experimental conditions ($p = 1.6$ µm; $R = 25$ µm). This value was systematically subtracted from the measured coordination numbers.

The relation between the mean coordination number and shrinkage ε is deduced from Eq. (14) by considering the uniform shrinkage of the particle packing [45]:

$$Z = Z_0 + 15.5\varepsilon \tag{16}$$

This expression was compared with our experimental values (Fig. 9a), and both calculated and experimental values are in good agreement. Errors in particle segmentation when particle impingements are large may be responsible for some discrepancies at high shrinkage. The distribution

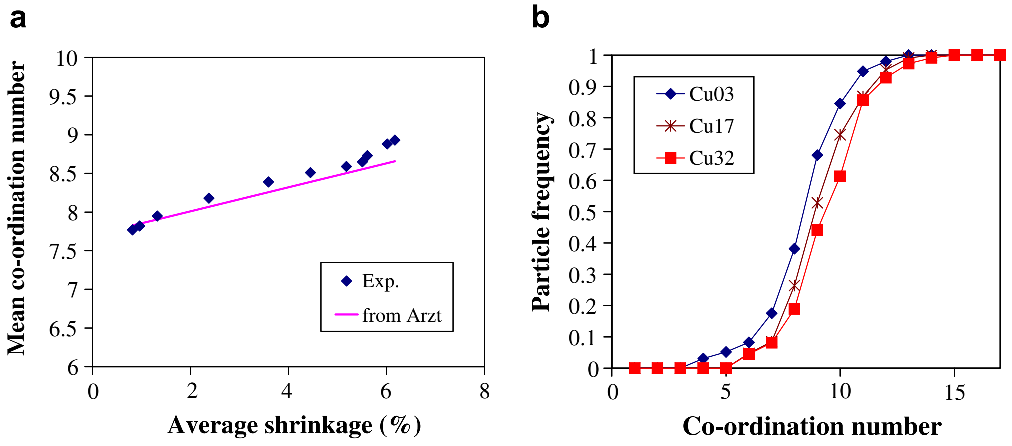

Fig. 9. Mean particle coordination number as a function of shrinkage (a) and distribution of coordination numbers at different stages of sintering (b) (the numbers correspond to the microtomographies referred to in Fig. 2).

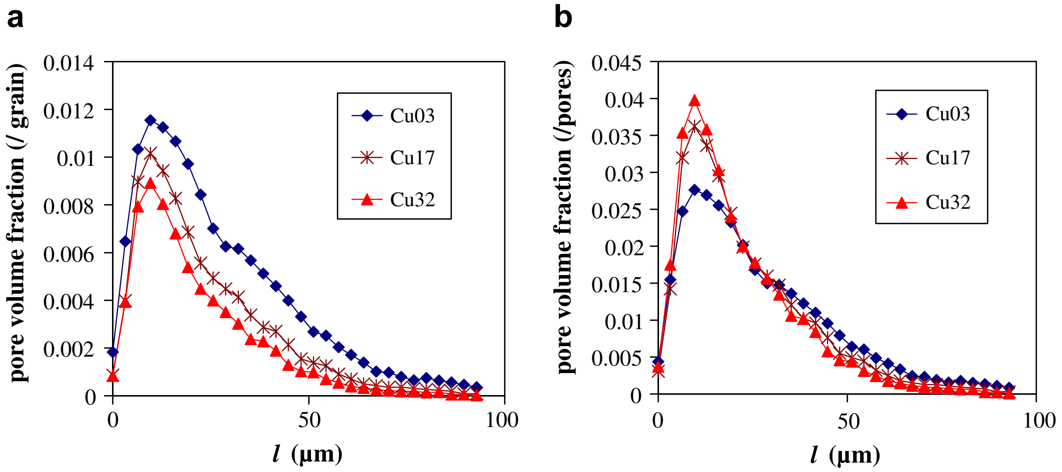

Fig. 10. Intercept length volume distributions in the pore phase at different stages of sintering (the numbers correspond to the microtomographies referred to in Fig. 2): (a) with respect to the grain volume; (b) with respect to the pore volume.

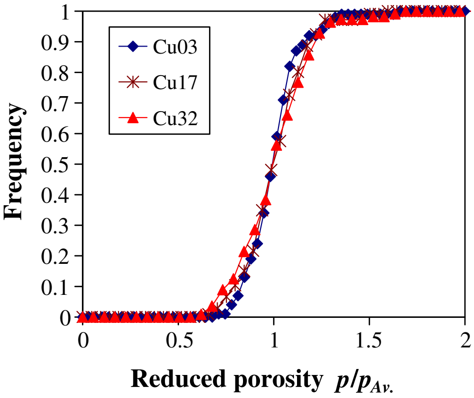

Fig. 11. Porosity distributions in influence cells (see Fig. 5) at different stages of sintering (the numbers correspond to the microtomographies referred to in Fig. 2).

of coordination number is globally shifted to higher values as sintering proceeds (Fig. 9b), i.e. the fraction of weakly coordinated particles decreases, whereas the fraction of highly coordinated particles increases.

Variation of the intercept length distribution in the pore phase shows a decrease in the pore volume in all size classes (Fig. 10a). The formation of large pores, which could have occurred due to differential shrinkage, is then not observed in the analysed volume. The pore intercept length distribution becomes narrower as sintering proceeds, as seen in the distributions normalized by the total pore volume (Fig. 10b). A slight variation of the reduced porosity distribution in influence cells is, however, reported (Fig. 11): the porosity ratio between the highly porous areas and the denser areas increases as sintering proceeds, which is the sign of a non-uniform densification in the compact.

4. Discussion

The experimental system under study was a packing of Cu spherical particles whose initial density is characteristic of a random close packing (green density ≈ 0.68). Packing heterogeneity is always present in a random particle packing, but it is minimized in a random close packing. It is therefore important to know how the mean field approach can apply to this system where shrinkage is rather uniform compared to what is observed in most particle packings. In situ microtomography of the powder compact during sintering made it possible to track the variation of average microstructural characteristics in a given reference volume. Particle rearrangement, which could result from thermal cycling if analyses were performed on annealed/quenched samples, is then avoided.

A statistical approach of the variation of local microstructural characteristics was performed from the 3D images, i.e. the results were obtained by averaging local measurements inside a given volume which was followed throughout sintering. Tracking the variation of each local configuration was beyond the scope of this work and would be its natural continuation. Edge effects were corrected by adapting the usual methods of 2D image analysis, so that there is no bias in the analysis resulting from the bounded character of the analysed volume. Precision in the analysis is then limited only: (i) by the statistically representative character of the reference volume and (ii) by systematic errors in the size of small features, near the limit of the voxel size. A few hundred particles were followed in the reference volume. The measured average density in this volume is consistent with the measured average density in the three times larger embedding volume (Fig. 7), which tends to indicate that the reference volume is representative of the compact. The main issue concerning the resolution was in the analysis of neck sizes and coordination numbers in our work. The difficulty in differentiating between true contacts and neighbouring surfaces induced a systematic overevaluation of the contact sizes and coordination numbers, even for necks which are large compared with the voxel size, due to the small surface curvature (see Eq. (6)).

Most results do not show any significant discrepancy with conventional descriptions of uniform shrinkage of a particle compact: the neck growth and densification kinetics agree with the 2-Sphere model, within the range of accessible experimental data; the increase in coordination number is consistent with Arzt's model, which assumes a uniform centre-to-centre approach; and the opening of large pores (absolute volume increase), which was sometimes observed in the initial stage and at the beginning of the intermediate stage of sintering, is not observed here. The effect of microstructural heterogeneity on the variation of average characteristics of the packing is then hardly detectable in our experiments. Only the variation of local porosity in influence cells of each particle evidences a slight trend to increase the fraction of relatively large porous zones and the fraction of relatively dense zones, which is the sign of a not completely uniform densification. A recent study by X-ray tomography also focused on rearrangement effects during sintering of copper spherical particles [33]. The measured cumulative particle rotations remained lower than 2° during sintering and heating/cooling cycles in this study, which indicates a very limited particle rearrangement.

5. Conclusion and outlooks

X-ray microtomography was used to follow in situ the sintering of a copper powder, with close particle packing. A statistical analysis of the local 3D microstructure was performed. For the first time, a complete set of morphological characteristics of the 3D particle packing have been determined and followed throughout sintering. The average microstructural changes (neck size, coordination number, pore size distribution) and the densification kinetics are in agreement with the predictions of the mean field sintering models, which assume a uniform shrinkage of the powder compact. Only the variation in the local porosity distribution is a sign that densification is not completely uniform. The results confirm previous experimental 2D image analyses, pore size distribution analyses from physical methods and results of discrete element models, which report that the effect of microstructural heterogeneity on the average microstructural and macroscopic characteristics of the particle packing are significant only with low-density green compacts. Deviation from the mean field models remain limited during sintering of a random close particle packing, where microstructural heterogeneity is weak. More heterogeneous systems will be investigated in the future, such as particle packings with large pores or solid inclusions. Further work will also aim to track local changes in particle packing configurations and thus quantify particle rearrangement.

Aknowledgements

The contribution of A.V. has been allowed thanks to the financial support of the European Commission through PM-MACH Growth Project (No. GRD1-2001-40775).

References

[1] Herring C. The physics of powder metallurgy. New York: McGraw Hill; 1951.
[2] Kuczynski GC. Trans AIME 1949;185:169–78.
[3] Kingery WD. J Appl Phys 1959;30(3):301–6.
[4] Coble RL. J Appl Phys 1961;32(5):787–92.
[5] Ashby MF. Acta Metall 1974;22:275–89.
[6] Swinkels FB, Ashby MF. Acta Metall 1981;29:259–81.
[7] Jagota A, Dawson PR. Acta Metall 1988;36(9):2551–61.
[8] McMeeking RM, Kuhn LT. Acta Metall Mater 1992;40(5):961–9.
[9] Du ZZ, Cocks ACF. Acta Metall Mater 1992;40(8):1969–79.
[10] Svoboda J, Riedel H, Zipse H. Acta Metall Mater 1994;42(2):435–43.
[11] Raj R, Bordia RK. Acta Metall 1984;32(7):1003–19.
[12] Kim H, Gillia O, Dorémus P, Bouvard D. Int J Mech Sci 2002;44:2523–39.
[13] Kraft T, Riedel H. J Eur Ceram Soc 2004;24(2):345–61.
[14] Petzow G, Exner HE. Z Metallkd 1976;67(9):611–8.
[15] Huppmann WJ, Riegger H, Petzow G, Kolar D. Sci Ceram 1977;9:67–74.
[16] Weiser MW, De Jonghe LC. J Am Ceram Soc 1986;69(11):822–6.
[17] Chermant JL, Coster M, Jernot JP. Modern Develop Powder Metall 1981;12:377–89.
[18] Missiaen J-M. Mater Sci Eng A 2007.
[19] Aigeltinger EH, DeHoff RT. Metall Trans A 1975;6A:1853–62.
[20] Zheng J, Reed JS. J Am Ceram Soc 1989;72(5):810–7.
[21] Hsieh HL, Fang TT. J Am Ceram Soc 1990;73(6):1566–73.
[22] Chen PL, Chen IW. J Am Ceram Soc 1996;79(12):3129–41.
[23] Allen AJ et al. J Am Ceram Soc 1996;79(5):1201–12.
[24] Kingery WD, François B. In: Kuckzinsky GC, editor. Sintering and related phenomena. Gordon and Breach, New York; 1967. p. 471—98.
[25] Jagota A, Dawson PR. Acta Metall 1988;36(9):2563–73.
[26] Parhami F, McMeeking RM. Mech Mater 1998;27:111–24.
[27] Lee S-M, Chaix J-M, Martin CL, Allibert CH, Kang S-JL. Met Mater 1999;5(2):197–203.
[28] Martin CL, Schneider LCR, Olmos L, Bouvard D. Scripta Mater 2006;55(5):425–8.
[29] Henrich B, Wonisch A, Kraft T, Moseler M, Riedel H. Acta Mater 2007;55(2):753–62.
[30] Lame O, Bellet D, Di Michiel M, Bouvard D. Acta Mater 2004;52(4):977–84.
[31] Di Michiel M et al. Rev Sci Instrum 2005;76(4):043702-1.
[32] Bernard D, Gendron D, Heintz J-M, Bordere S, Etourneau J. Acta Mater 2005;53(1):121–8.
[33] Nöthe M et al. In: Eun KY, Kim YS, editors. Powder metallurgy world congress (PM2006). Busan (Korea): Korean Powder Metallurgy Association; 2006. p. 808–9.
[34] Serra J. Image analysis and mathematical morphology, vol. I. London: Academic Press; 1982.
[35] Missiaen JM, Roure S. J Microsc 2000;199:141–8.
[36] Coster M, Chermant JL. Précis d'analyse d'images. Paris: CNRS; 1989.
[37] Beucher S, Vincent L. Traitement d'images en microscopie à balayage et en microanalyse par sonde électronique. Paris: ANRT; 1990. p. F-1.
[38] Serra J. Acta Stereol 1995;14(2):99–111.
[39] Kang S-JL. Sintering. Oxford: Elsevier; 2005.
[40] Johnson DL. J Appl Phys 1969;40(1):192–200.
[41] German RM. Powder metallurgy science. Princeton (NJ): Metal Powder Industry Federation; 1994.
[42] Gregg RA, Rhines FN. Metall Trans A 1973;4:1365–74.
[43] Jernot JP. Ann Chim 1985;10:319–30.
[44] DeHoff RT, Rhines FN. Quantitative microscopy. New York: McGraw Hill; 1968.
[45] Arzt E. Acta Metall Mater 1982;30:1883–90.